Densification modeling for gas pressure sintered silicon nitride-based ceramics with Thermo-Optical dilatometry

Thomas Grippi, Stéphanie Béhar-Lafenêtre, Holger Friedrich, Daniel Haas, Uwe Schenderlein, Sylvain Marinel, Charles Manière

Densification modeling for gas pressure sintered silicon nitride-based ceramics with Thermo-Optical dilatometry

Thomas Grippi[1,2]*, Stéphanie Béhar-Lafenetre[1], Holger Friedrich[3], Daniel Haas[4], Uwe Schenderlein[4], Sylvain Marinel[2], Charles Manière[2]*

1. Thales Alenia Space, 5 Allée des Gabians, 06150, Cannes, France
2. CRISMAT, Normandie Univ, ENSICAEN, UNICAEN, CNRS, 14000, Caen, France
3. Fraunhofer-center HTL 95448 Bayreuth, Germany
4. QSIL Ingenieurkeramik 96528 Frankenblick, Germany

Keywords
Silicon nitride, Si_3N_4, Gas pressure sintering, Densification, model, Thermo-optical measurement

Abstract

The complexity of gas pressure liquid phase sintering (GPS-LPS) of silicon nitride induces a certain *savoir-faire*. This highly challenging strong bond ceramic uses sintering additives of a liquid phase sintering under high temperatures close to the silicon nitride phase decomposition which requires a gas pressure. The sintering behavior encompasses various phenomena such as Ostwald ripening grain growth, phase transition, and swelling when the pore elimination approach close porosity. The aim of this study was to model such sintering behavior. In this aim, master sintering curves (MSC) were used to study the temperature and porosity dependence of the sintering model. Then, the grain growth sensitivity of the sintering model was incorporated. Finally, the swelling phenomenon responsible for transient de-densification and sintering rate limiting mechanism at final stage sintering was extracted by an inverse method. A comprehensive sintering model reproducing all the silicon nitride sintering complexity result this study.

Graphical Abstract

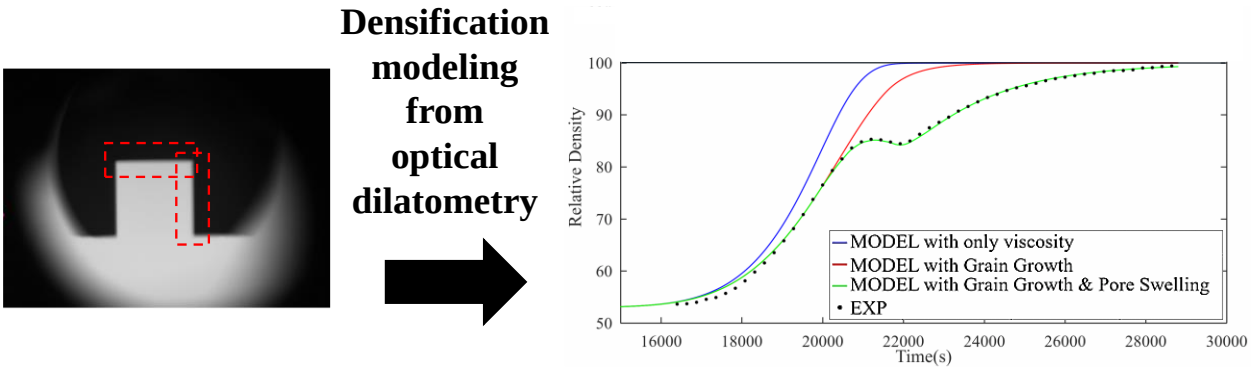

* Corresponding author:
Charles Manière, Laboratoire CRISMAT
6 Boulevard du Maréchal Juin 14000 CAEN, France
E-mail address: charles.maniere@ensicaen.fr

Highlights

- Gas pressure liquid phase sintering of silicon nitride
- Sintering kinetics analysis from optical dilatometry
- Comprehensive simulation of sintering with a sensitivity to grain growth and swelling phenomena

Nomenclature

θ Porosity
$\dot{\theta}$ Porosity elimination rate (s^{-1})
$\underline{\sigma}$ Stress tensor ($N.m^{-2}$)
$\underline{\dot{\varepsilon}}$ Strain rate tensor (s^{-1})
$\dot{e}$ Trace of the strain rate tensor (s^{-1})
φ Shear modulus
ψ Bulk modulus
P_l Sintering stress (Pa)
$\mathbb{i}$ Identity tensor
α Surface energy ($J.m^{-2}$)
r Mean particle radius (m)
η Material viscosity (Pa.s)
η_0 Viscosity pre-exponential factor (Pa.s)
Q Viscosity activation energy ($J.mol^{-1}$)
R Gas constant 8.314 ($J.mol^{-1}.K^{-1}$)
T Temperature (K)
$\dot{G}$ Grain growth rate ($m.s^{-1}$)
G Grain size diameter (m)
G_0 Initial grain size diameter (m)
p Grain growth rate exponent
K Grain growth factor ($m^{1+p}.s^{-1}$)
k_0 Grain growth pre-exponential factor ($m^{1+p}.s^{-1}$)
Q_G Grain growth activation energy ($J.mol^{-1}$)
m Viscosity grain size exponent
C_0 Constant
w Sintering equation grain size exponent
$f(\theta)$ Sintering model porosity function
D Relative density
h Specimen height (mm)
D_{final} Final relative density
h_{final} Final specimen height (mm)

1. Introduction

Si_3N_4 based ceramics are commonly used for stable structures in space application components due to its attractive properties: Low density, stable in harsh environment, outstanding mechanical properties[1–3]. Furthermore, silicon nitride ceramics are known for their low coefficient of thermal expansion, their stiffness and their high strength[4–7]. Nevertheless, because of its high degree of covalent bonding between silicon and nitrogen, obtaining fully dense parts of the pure phase by pressure-less sintering process is very difficult. Consequently, sintering methods including the application of pressure have been adapted to silicon nitride: Hot Isostatic Pressing (HIP)[8,9], Spark Plasma Sintering (SPS)[10]. However, the pressure-assisted sintering of pure phase remains difficult and the most efficient way to obtain both high temperature properties and the possibility to obtain complex shapes was the use of nitrogen Gas Pressure Sintering (GPS)[11,12], combined with a Liquid Phase Sintering (LPS) approach. Different sintering additives have been tested[7,13–16] such as MgO, SiO_2, Y_2O_3, Al_2O_3 but the most used additives showing optimal properties at high temperature are Y_2O_3 and Al_2O_3[16–18]. GPS sintering of such material results in a fully dense microstructure with elongated silicon nitride grains having interesting mechanical properties flexural strength (~730 MPa) and toughness (~10.6 $MPa \cdot m^{1/2}$)[19]. Nonetheless, as applied to complex and large parts for space industry, such liquid phase sintering technic involves low viscosity at high temperature which raises the sintered specimen sensitivity to distortions[20] as well as cracks or remaining macro-porosity. Therefore, the minimization and the anticipation of the risk of occurrence of these defects are main objectives for industries. The simulation of the sintering behavior by the continuum mechanic is a key tool to anticipate these defects. In addition, the microstructure development of Si_3N_4 GPS-LPS sintering is complex and involves Ostwald ripening based grain growth through the liquid phase, phase

changes, and swelling phenomenon at the moment of pore closure. The latter may interact with the densification behavior and should be considered in the sintering model. To be able to implement such a comprehensive model for Si_3N_4 GPS-LPS sintering, it is required to identify a range of physical parameters including the grain growth, effective viscosity, sintering moduli, the identification of the dominant densification mechanism and the swelling pressure[21–24].

The difficulty of studying Si_3N_4 GPS-LPS sintering is the high temperatures involved and the gas pressure which make typical dilatometry investigations difficult. The main interest of this article is the identification of the sintering parameters from optical dilatometry on different heating rate cycles, reaching the same holding sintering temperature. These parameters extraction has for objective the conception of an analytical model based on Skorohod-Olevsky continuum theory of sintering that is implementable in finite element sintering simulation tools. This study details the method adopted from the multiple sintering parameters extraction of the linear-viscous porous model by taking into account the densification kinetics and the effect of grain growth and swelling pressure phenomena.

2. Experimental Procedure

The furnace used for the study is located at the Fraunhofer Center HTL in Bayreuth. It is named TOM_Metal, for “Thermo Optical Measuring”[25]. TOM_Metal is a vertically placed cylindrical furnace. The heating is provided by graphite rods located vertically at the periphery of the furnace and its top and base sections are water-cooled. The studied material is a grade of silicon nitride powder mixture that has been provided and is property of QSIL. The actual composition of the grade includes 90% of Si3N4 with 10 % Y2O3 / Al2O3 as sintering additives of this silicon nitride ceramic grade SN-GP. The studied samples are debinded cold isostatic pressed cylinders of ø10×10mm. The green density of the isostatically compacted samples is 1.88g/cm3 for a theoretical density of 3.18g/cm3. At the end, the final density after sintering has been measured with 3 weighing Archimedes method and respects the industrial’s standards with almost fully dense samples and less than 1% residual porosity. The mean longitudinal grain size has been measured to be 1µm.

The studied samples are placed into 2 interlocked graphite crucibles one with windows for the camera (TOM) dilatometry devices that follows the specimen sintering and another control sample in a fully closed crucible. The sample is surrounded by “scrap material” (crushed silicon nitride elements made of the same composition as the sample) to mimic the sintering conditions in an industrial furnace where several parts are simultaneously produced.

The device can support samples sized from 5mm to 35mm with a 0.3 µm resolution. The ø10x10mm cylinders for the study are fitting to these requirements in order to have the best dilatometry resolution possible.

As can be inferred from the drawing below (Figure 1) the CCD camera is oriented through the window where the sample is placed. At low temperature, an Ulbricht sphere light is used as a

backlight to be able to measure and to calibrate the sample. At 1200°C, the silicon nitride sample starts to emit in the visible, the back light is switched off. Evidently, as the camera is measuring a 2D shape variation, the shape of the sample must be cylindrical to avoid distortions (see Figure 2).

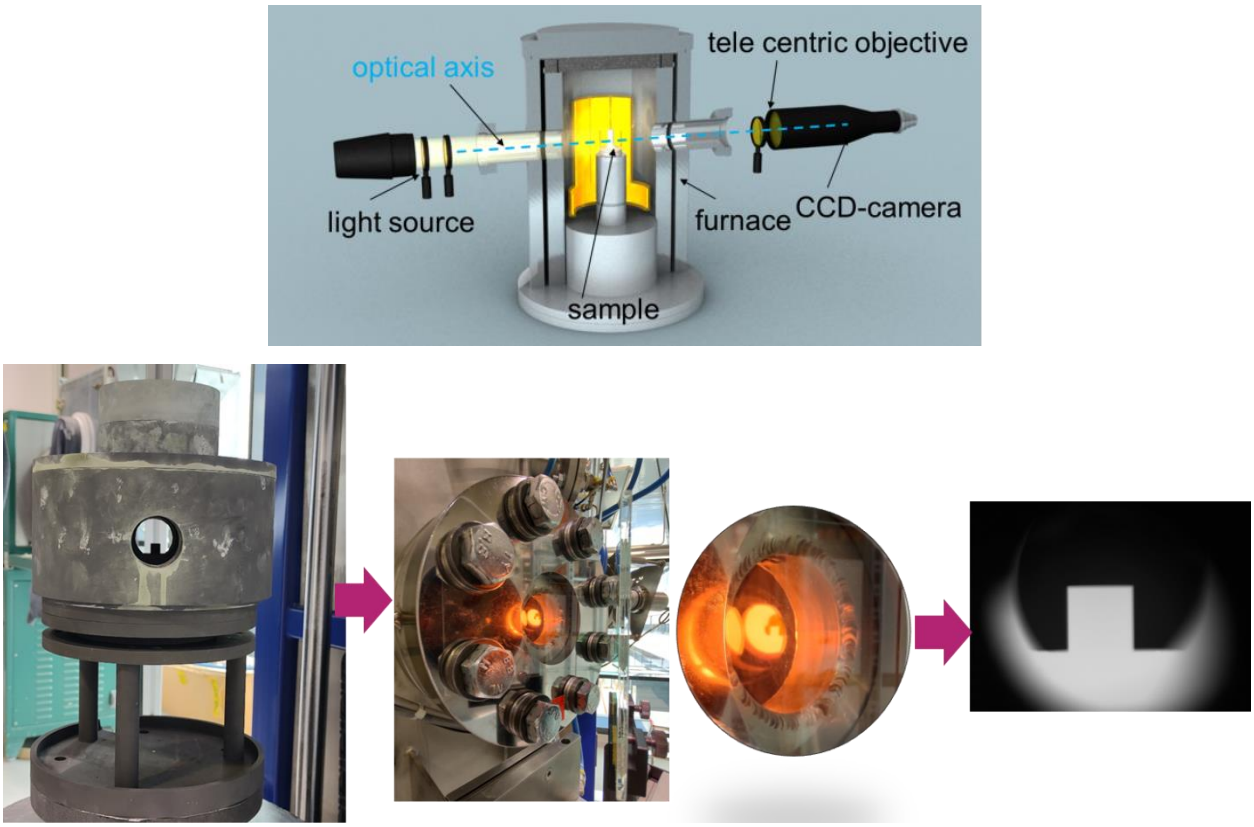

Figure 1 Schematic view of the furnace and optical dilatometry configuration. (Pictures with courtesy of Fraunhofer-Center HTL)

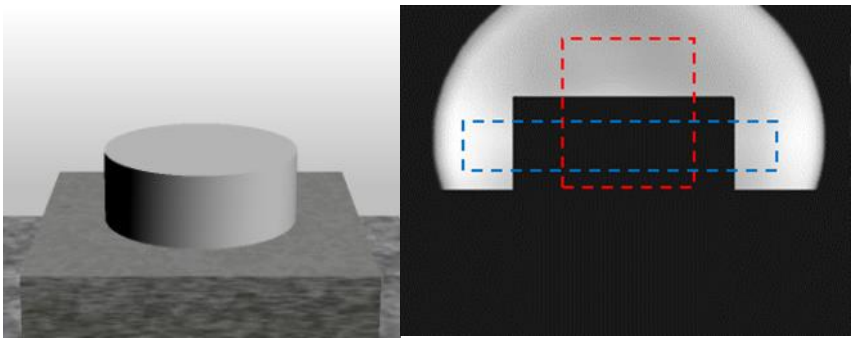

Figure 2 Sample dimension limits (left) and ideal geometry (right) for Thermo-Optical measurements. (Pictures with courtesy of Fraunhofer-Center HTL)

3. Results and discussions

3.1. Experimental analysis of the sintering densification behavior

The following part is depicting the extraction of the sintering behavior of Si_3N_4 from dilatometry data. This study needs the experimental exploration of the sintering under different heating rates to extract the sintering kinetic parameters during the various sintering stages.

These explorations are based on a kinetic field approach [23,24]. The sintering behavior of silicon nitride has been studied in 3 different cycles with 3 heating rates: 2.5 K/min, 5 K/min and 10 K/min. From dilatometric curves recorded by the TOM device (see Figure 3), the densification curves can be extracted by the formula $D=D_{final}(h_{final}/h_t)^3$ assuming homothetic densification. From the densification kinetic data, the sintering activation energy and the viscous moduli were identified by a combination of kinetic field method [23,26], and a calibration of the moduli [27,28]. As can be observed on Figure 3, densification follows the heating rate (the higher the heating rate is, the higher the densification rate is). An unusual behavior is observed when density is ranging from 80 to 85 % of the theoretical density (near close porosity): a swelling appears (transient de-densificatio). The observed geometric variation is about 0.02mm for our 10mm cylinder sample. Thus, densification slows down and swelling phenomenon appears, which will be detailed in the further section.

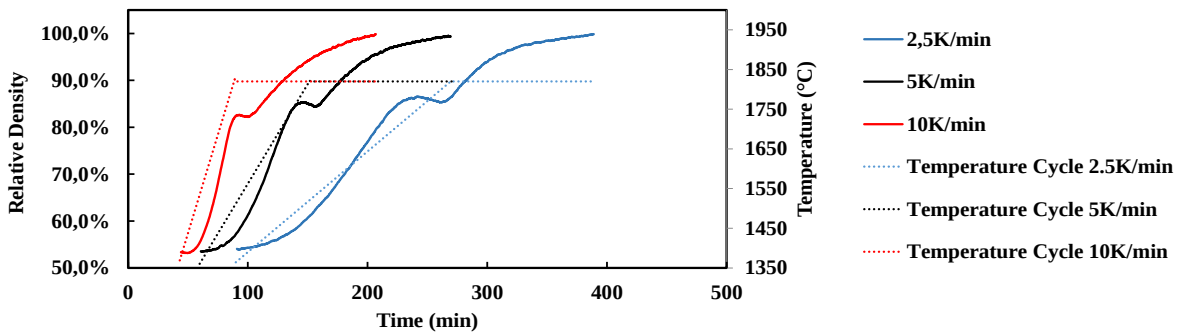

Figure 3 3 cycles with different heating rates and 3 densification responses on TOM Metal at the Fraunhofer Center HTL.

On the graph Figure 4, relative density *versus* temperature is plotted, it can be seen that the swelling does not appear exactly at the same temperature like a rate controlling mechanism. The slower the heating rate is, the sooner in temperature the swelling appears.

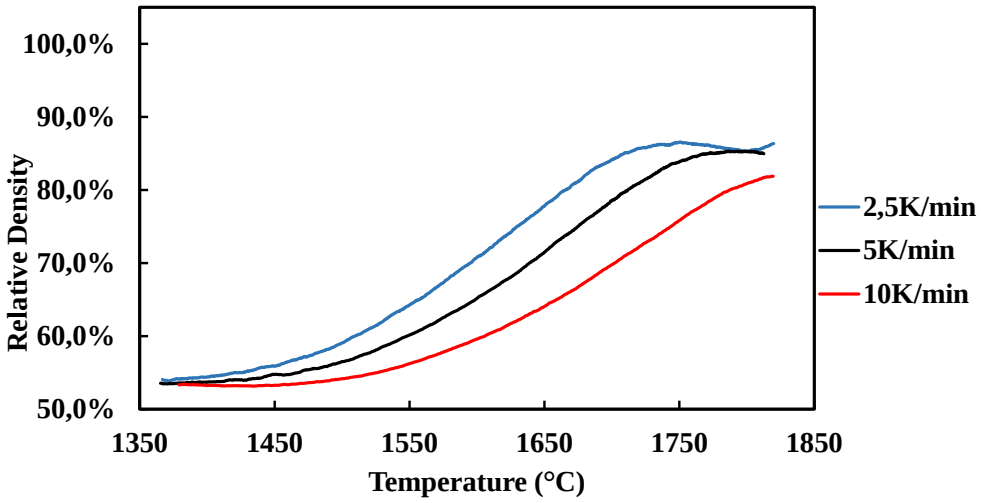

Figure 4 Relative density as a function of temperature, during the heating, for 3 different heating rates on TOM Metal at the Fraunhofer Center HTL.

3.2. Different possible origin of the apparent swelling phenomenon

3.2.1. Swelling from α to β phase transformation

In a phase transformation, swelling can result from a change in the volumetric mass of the two involved phases. The silicon nitride sintering starts from α phase powders and ends in nearly full transformed β phase, at the end of the sintering as shown on the XRD patterns, Figure 5. However, this transformation does not explain the swelling phenomenon for two reasons. The specific weight of the phases α and β, are $3.18 g \cdot cm^3$ and $3.2 g \cdot cm^3$, respectively, which are very close. The α to β transformation does not imply volumetric mass variation, therefore the swelling phenomenon cannot be explained by it. Another reason is the fact that the swelling phenomenon does not seem to appear at the same temperature as a phase transformation does. It seems to be more dependent on the heating rate. The two other swelling mechanisms are then preferred as potential explanation.

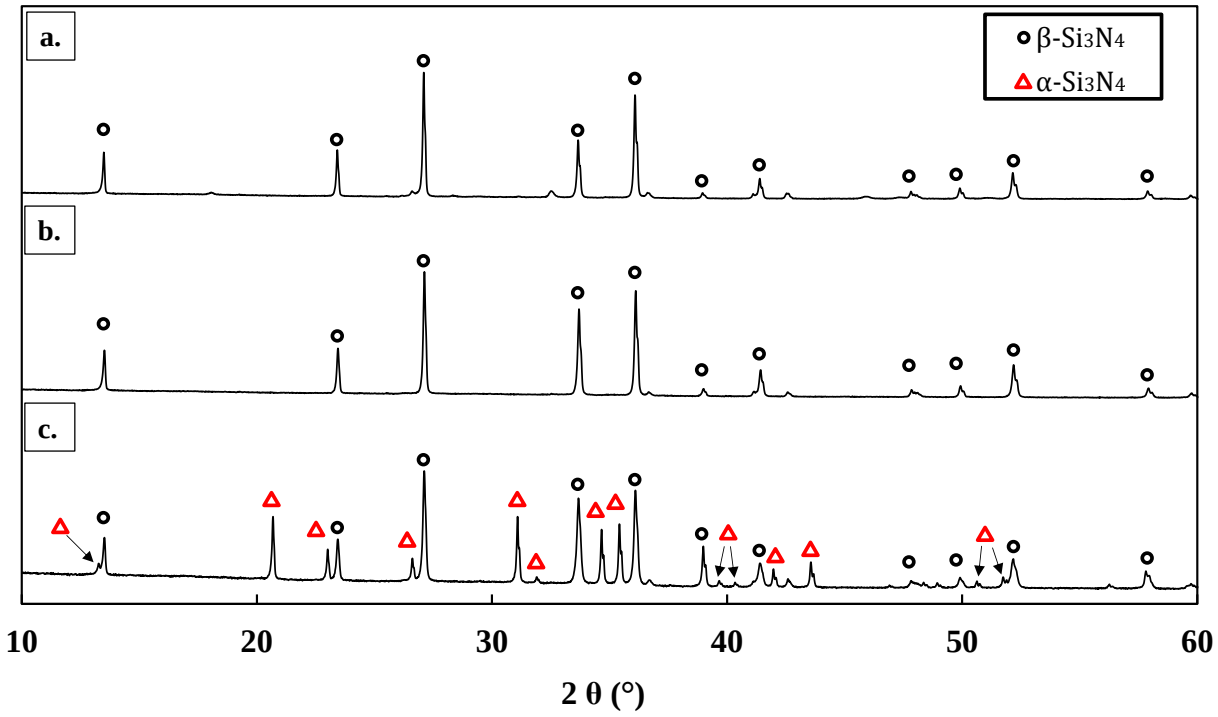

Figure 5 X ray diffraction of the powder and the sintered specimens. Quenches at 1820°C for 30min (a.), 1820°C for 0min holding (b.) and 1720°C for 0min holding (c.).

3.2.2. Swelling Phenomenon by Pore Coalescence

As observed before from the density curves, the pore swelling is a mechanism that slows the densification and that appears when pores are closing. In addition it is well known, that the nitrogen gas is soluble in the liquid phase allowing gas transports between the pores[29]. These exchanges of gas between the small pores (more compressed by capillarity) and then highly energetic toward larger pores less energetic imply a pore coarsening phenomenon that results in larger pores (Figure 6). This larger pore also implies a swelling because for a same pore gas quantity (from small pores) the equilibrium with capillarity forces makes the pore volume bigger for a higher pore diameter. This phenomenon is highly active for partially soluble gas and is often observed for liquid phase sintering like porcelain sintering [30].

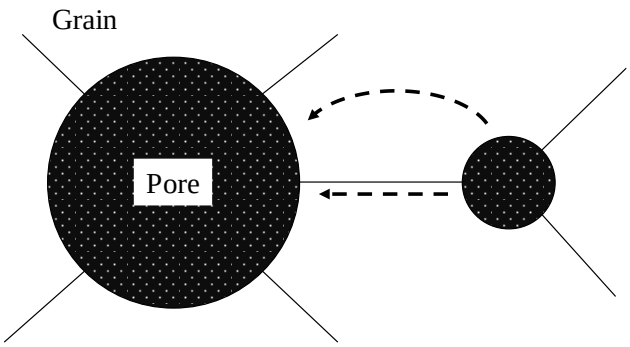

Figure 6 Scheme of the pore gas migration in pore coalescence swelling mechanism.

This pore coalescence mechanism is one potential candidate in explaining the swelling in liquid phase sintering of silicon nitride. In Figure 7, the low magnification SEM analysis before, during

and after the swelling (*via* the tests at different heating rate) clearly shows the formation of large pore during swelling which could correspond to a pore coalescence swelling mechanism.

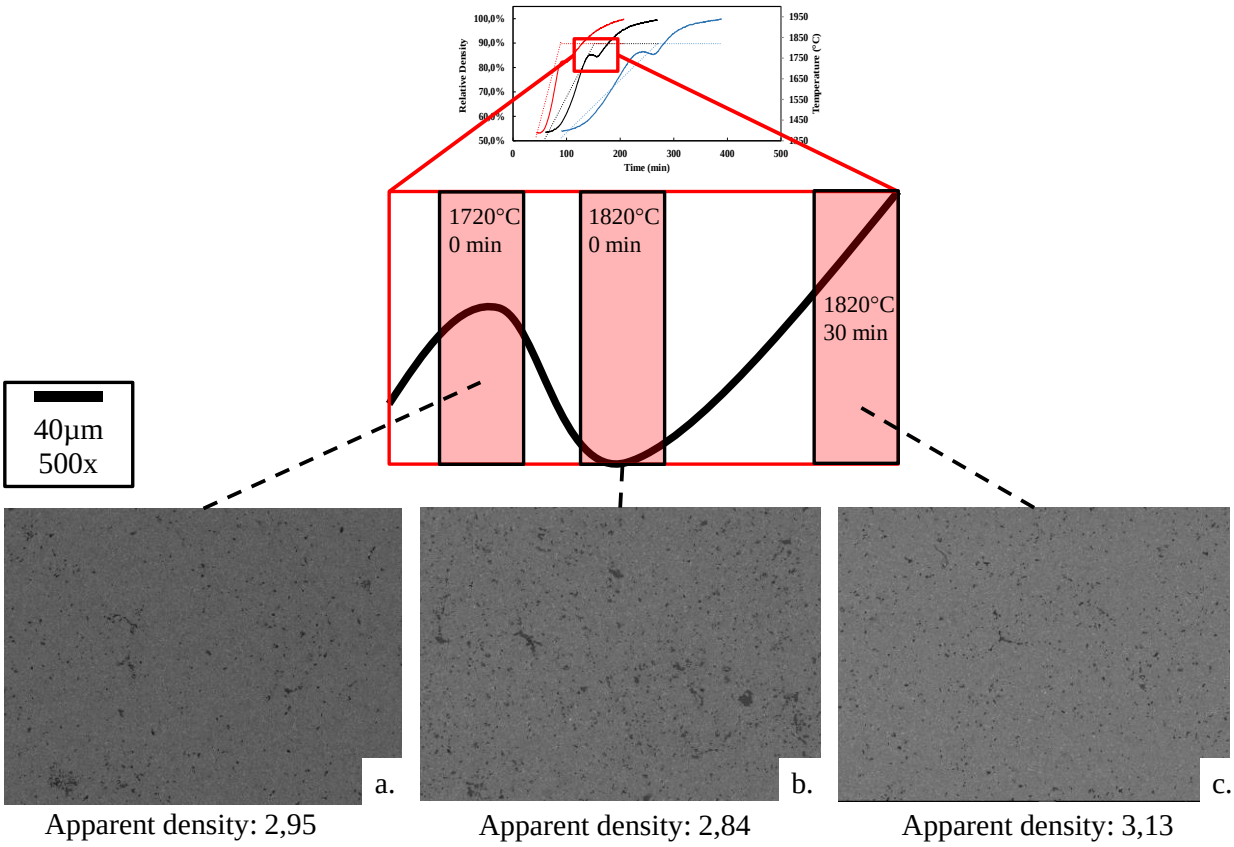

Figure 7 SEM Micrographs in the swelling zone.

3.2.3. Non-equiaxes grain growth and swelling

Another mechanism that could explain the swelling phenomenon is the non-equiaxed grain growth. One of the particularities of silicon nitride is the presence of an allotropic α/β phase transition during sintering which leads to the generation of non-equiaxed grains (β)[6,31,32]. The presence of these non-equiaxed grains is essential to the particular mechanical properties of silicon nitride (high toughness). Moreover, a sintering “shrinkage accident” (transient de-densification) appears at high temperature (about 1800°C).

Analogously as in non-stoichiometric barium titanate[33] or undoped alumina cases[34], a swelling phenomenon could appear by the end of sintering. This phenomenon is explained by the creation of a new geometry of large and non-equiaxed grains (not associated with an allotropic transition in the case of these ceramics). This new generation invades the microstructure by being supplied by a generation of smaller equiaxed grains by the mechanism of Ostwald ripening, and, finally, can lead to a transient de-densification by a de-cohesion mechanism.

The XRay diffraction analysis performed on the same quenched sample, shown on Figure 5, highlights the presence of the 2 phases, alpha and beta in the first sample (c.), whereas no α-Si_3N_4 traces have been found in the following quenched (a. and b.). Once this transition is completed, most small grains coalesce into bigger grains and the presence of a liquid phase at high temperature allows the densification to continue. The SEM image of pores in Figure 8, shows bridging non-equiaxed grain which could explain a decohesion swelling mechanism.

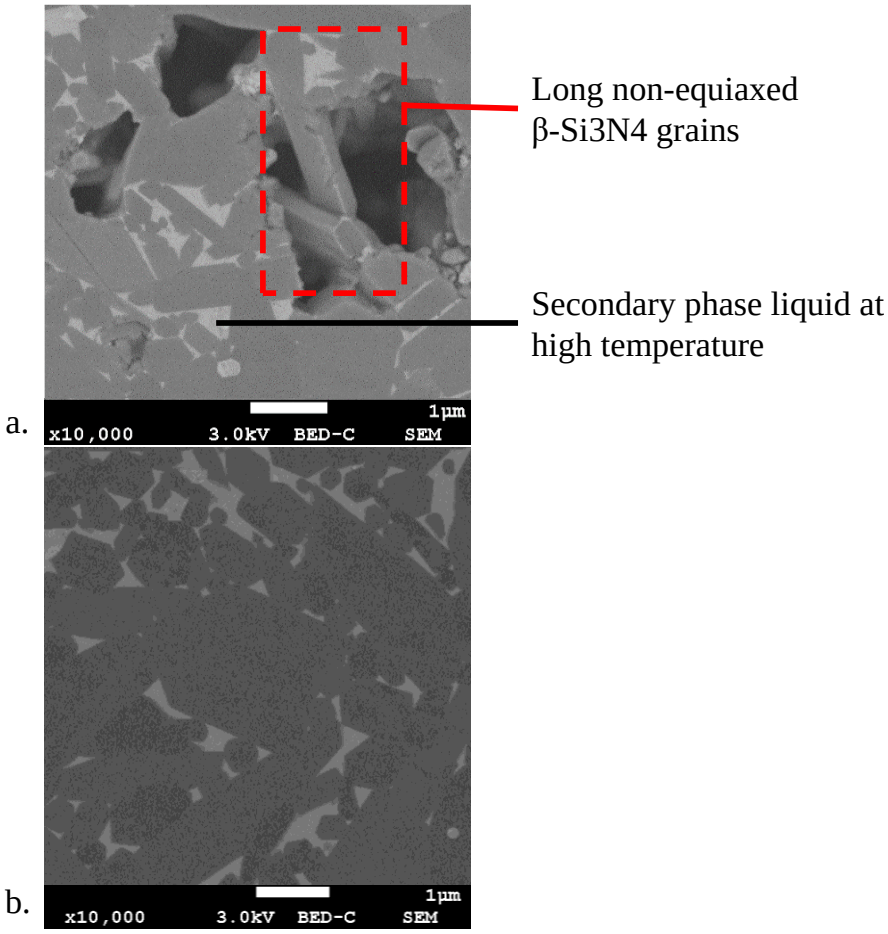

Figure 8 Micrographs showing the microstructure from a sample after a sintering cycle at 1820°C with 30min holding (a.) and a comparison of the dense microstructure after a sintering cycle at 1820°C and 2h holding (b.).

Both pore coalescence and de-cohesion mechanisms may explain the swelling phenomenon. It is even possible that both mechanisms coexist. From a mechanistic point of view, both last swelling mechanisms imply a pressure exerted on the porous skeleton that opposes the sintering driving forces. In this article the swelling pressure is then determined indirectly by the delays, it generates in the densification mechanisms. An inverse approach is used to determine empirically the swelling pressure.

3.3. Strategy of analytic model identification of the GPS LPS sintering

The strategy of step-by-step identification of the previously described complex sintering behavior encompasses the following steps (represented in Figure 9):

-Case 1: The typical sintering model considering only the sintering capillary forces and the linear-viscous porous material behavior is first determined in the zone of open porosity and low grain growth. The 3-heating rate procedure is first exploited to determine the sintering activation energy by kinetic field approach and then the pre-exponent factor is determined by a second linear regression approach. In this regression approach the sintering moduli are adjusted from Skorohod's [35] theoretical formulas to reproduce the activation energy independently determined by kinetic field.

-Case 2: In a previous study, the grain growth kinetic has been determined[36]. With this data the same identification method is conducted and the sintering is corrected to better fit the intermediate sintering behavior that now takes into account the grain growth.

-Case 3: Final stage sintering requires the determination of the experimental swelling curve. In order to determine the latter, the analytic sintering model is inverted and the swelling pressure (Pswell) is isolated. Once this Pswell curve is obtained by this inverted approach, it is introduced in the final model that would perfectly fit the data points.

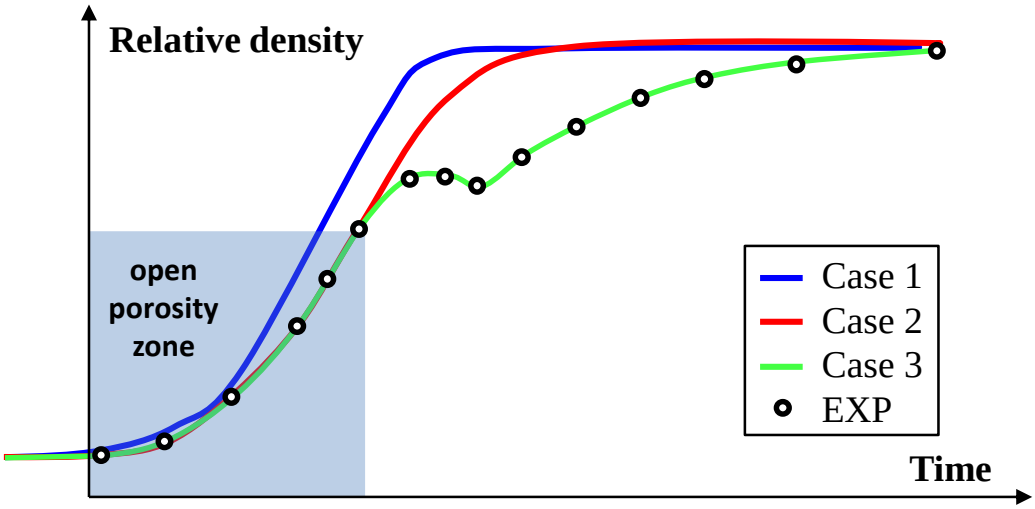

Figure 9 Scheme of the 3 stages sintering model identification.

3.1. Main sintering governing equations

Skorohod-Olevsky's continuum theory of sintering [35,37] general form is:

$$\sigma_{ij} = \frac{\sigma(W)}{W}\left(\varphi\dot{\varepsilon}_{ij} + \left(\psi - \frac{1}{3}\varphi\right)\dot{e}\delta_{ij}\right) + P_l\delta_{ij} - P_s\delta_{ij} \quad (1)$$

With σ_{ij} the externally applied stress tensor, $\frac{\sigma(W)}{W}$ generalized viscosity term, $P_l\delta_{ij}$ Sintering stress term, $P_s\delta_{ij}$the pore swelling pressure and $\left(\varphi\dot{\varepsilon}_{ij} + \left(\psi - \frac{1}{3}\varphi\right)\dot{e}\delta_{ij}\right)$ the material resistance term (Linear-viscous porous creep model).

In our particular case $\frac{\sigma(W)}{W}$ term is 2η for linear viscous behavior:

$$\underline{\sigma} = 2\eta\left(\varphi\underline{\dot{\varepsilon}} + \left(\psi - \frac{1}{3}\varphi\right)\dot{e}\mathbb{i}\right) + P_l\mathbb{i} - P_s\mathbb{i} \quad (2)$$

With the Skorohod theoretical shear and bulk moduli expressed as:

$$\varphi = (1-\theta)^2 \quad (3)$$

$$\psi = \frac{2}{3}\frac{(1-\theta)^3}{\theta} \quad (4)$$

3.1.1. Case 1: Isotropic, free sintering, without grain growth and pore swelling

Our first case, the “rough analytical model” is computed as a free/isotropic sintering but without taking into account the impact of grain growth or pore swelling. The general form can be simplified as:

$$0 = 2\eta\left(\varphi\underline{\dot{\varepsilon}} + \left(\psi - \frac{1}{3}\varphi\right)\dot{e}\mathbb{i}\right) + P_l\mathbb{i} \quad (5)$$

The mentioned sintering stress Pl is mainly driven by capillarity forces that can by estimated theoretically by Skorohod as:

$$Pl = \frac{3\alpha}{r}(1-\theta)^2 \quad (6)$$

Assuming no particle growth disturbance, we have:

$$Pl = \frac{3\alpha}{r_0}(1-\theta)^2 \quad (7)$$

From the computation of the mass conservation and the isotropic sintering, we have:

$$\dot{e} = 3\dot{\varepsilon}_r \quad (8)$$

$$\frac{\dot{\theta}}{1-\theta} = \dot{e} \quad (9)$$

We can simplify the reduced general expression by:

$$-P_l = 2\eta 3\dot{\varepsilon}_r\psi \Leftrightarrow \psi = \frac{-P_l(1-\theta)}{2\eta\dot{\theta}} \quad (10)$$

With 2η expressed as:

$$2\eta(T) = \frac{\eta_0}{\alpha}Texp(\frac{Q}{RT}) \quad (11)$$

The developed analytical model to be computed on Octave software can be expressed as:

$$\dot{\theta} = \frac{-P_l(1-\theta)}{\frac{\eta_0}{\alpha}Texp(\frac{Q}{RT})\psi} \quad (12)$$

3.1.2. Extraction of apparent activation energy Q

Two similar methods exist to determine independently the apparent activation energy by conducting different heating rate dilatometry. These methods are the Master Sintering Curve [21,28] and the kinetic fields method developed by Wang & Raj [23,24]. For this processing part, the house-made software SINTERLab. has been used. The input data are those recorded by the TOM metal system (Figure 4). Results from both MSC analysis and kinetic field method analysis give us an apparent activation energy of Q=350kJ/mol and Q=352kJ/mol respectively (see Figure 10 and Figure 11).

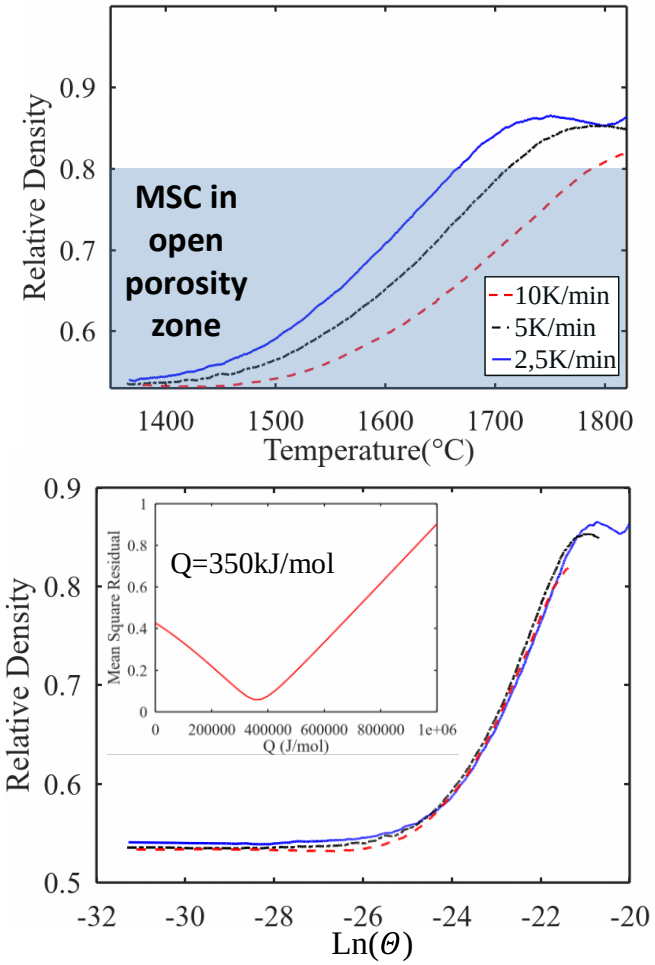

Figure 10 Master Sintering Curve on densification data with SINTERLab. Identification of apparent activation energy.

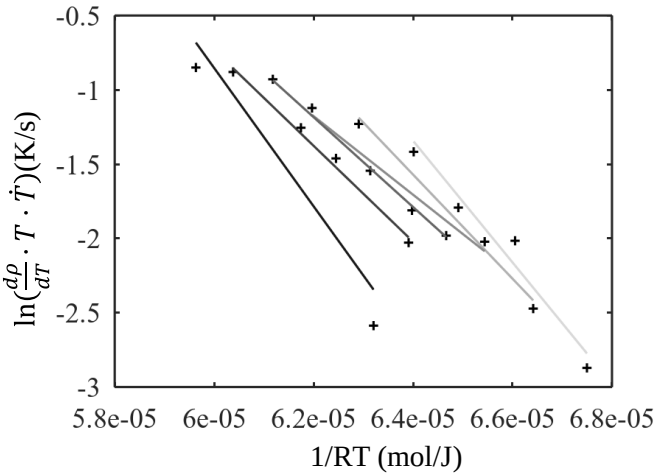

Figure 11 Kinetic fields method on densification data with SINTERLab. Identification of apparent activation energy.

3.1.3. Pre-exponential factor $\frac{\eta_0}{\alpha}$ identification

In a first attempt to determine the viscosity pre-exponential factor, we assume no grain growth. Based on the 5 K/min sintering cycle (which is the one to be simulated), the model developed in Equation (5) can be expressed to identify $\frac{\eta_0}{\alpha}$ with a linear regression [38]:

$$Y = \ln\left(\frac{-3(1-\theta)^3}{r_0 T \dot{\theta} \psi}\right) = \ln\left(\frac{\eta_0}{\alpha}\right) + \frac{Q}{RT} \quad (13)$$

From this linearization (Figure 12) assuming Skorohod's moduli, it is simple to extract the value of $\frac{\eta_0}{\alpha}$ by the curve origin and Q by the curve slope that should converge with the MSC and kinetic field results: Q=342857 J/mol and $\frac{\eta_0}{\alpha}$ = 0.068474. These values are not too far from the Q value identified by kinetic fields and therefore, they are used as first model.

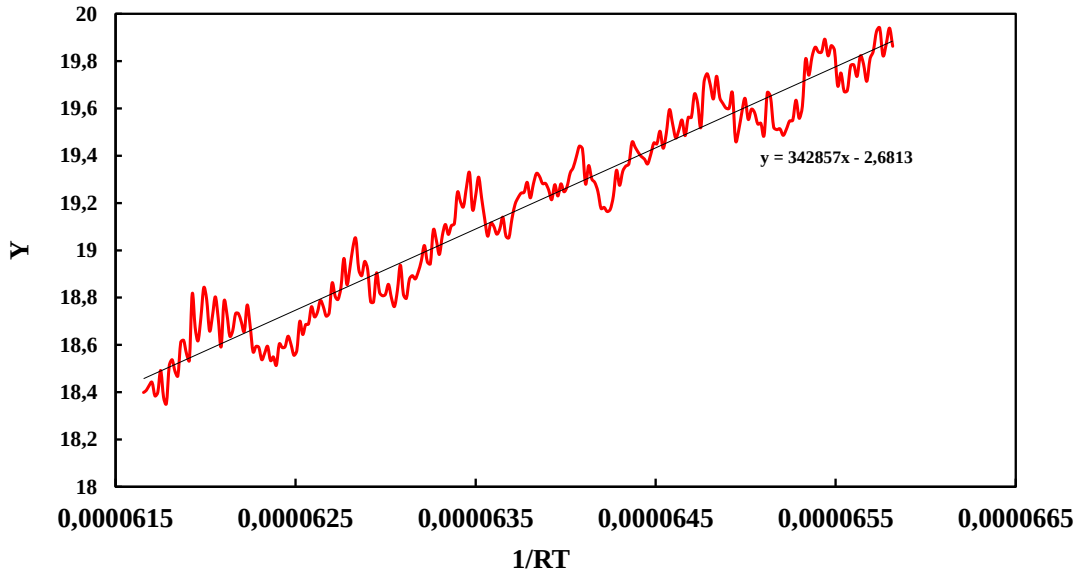

Figure 12 Linearisation of Y for identification of $\frac{\eta_0}{\alpha}$knowing the Apparent activation energy.

With these parameters, it is now possible to plot the behavior of the material and compare it to experimental values (Figure 13). This points out that the first model predicts the initial sintering behavior but fails in explaining the swelling and final relative densities. Taking into account the phenomena of grain growth and pore swelling depicted before is likely necessary.

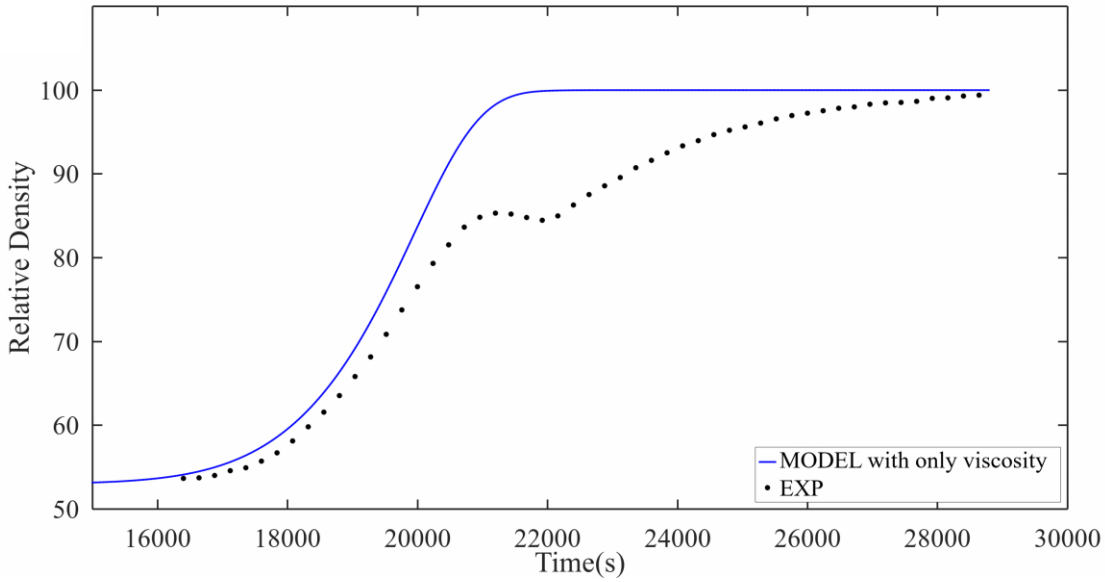

Figure 13 First sintering model and experimental values, based on identified parameters.

3.1.4. Adjustments of the Apparent Activation Energy taking into account the grain growth

The grain growth may influence the sintering kinetics from the beginning of the sintering, even in the range of open porosity. In this case, as can be seen with the developed model for grain growth [36], the grain growth seems to be effective in the studied zone for the method.

Therefore, it is preferable to model this parameter in the expression of Pl and to use the master sintering curve developed by Park et al. for viscous sintering [21] that takes this grain growth parameter into account (see Equation (14)).

$$\Theta_{vs}(t,T) \equiv \int_{t_0}^{t} \left(\frac{G_0}{G}\right)\frac{1}{T}\exp\left(-\frac{Q}{RT}\right)dt \qquad (14)$$

Identification of such parameter with this adjusted method gives Q= 340 kJ/mol (see Figure 14)

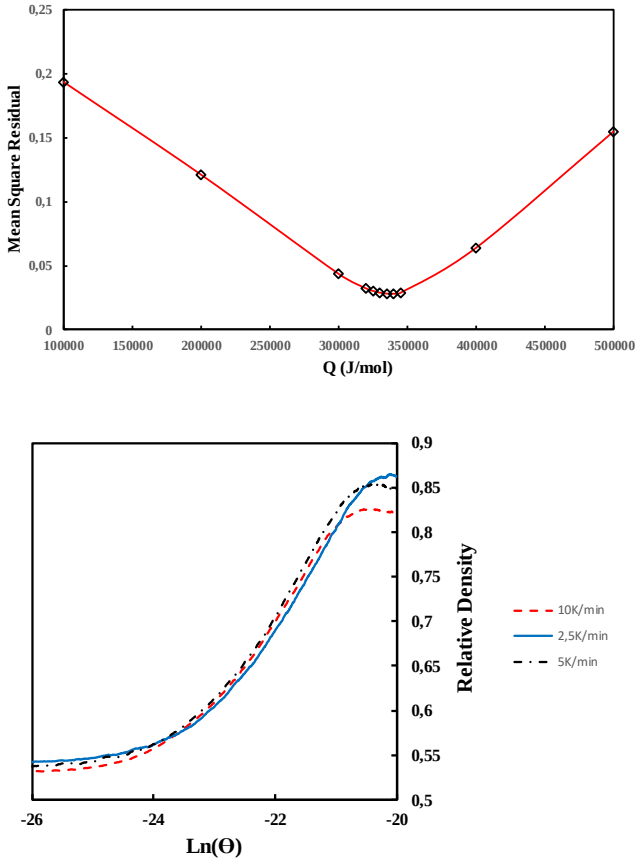

Figure 14 Master sintering curve method (Park model).

3.1.5. Pre-exponent factor determination to take into account grain growth kinetics

The MSC approaches give an activation energy Q independently from the porosity functions (like the bulk modulus) that are assumed to give a unique curve for all heating rates. For this case, the $\frac{\eta_0}{\alpha}$ can be identified with the updated linear regression equation that actualize the capillarity forces with the grain growth.

$$\ln(\frac{\eta_0}{\alpha}) + \frac{Q}{RT} = \ln(\frac{-6(1-\theta)}{T\dot{\theta}\psi G}) \quad (15)$$

In this expression the experimental bulk modulus function (16) is adjusted (playing on the θ_c and γ parameters) to have the linerisation slope corresponding to the MSC value of Q that is not influenced by porosity function unlike the regression approach.

$$\psi = \frac{2}{3}\frac{(\theta_c-\theta)^\gamma}{\theta} \quad (16)$$

From this linearization and the adjustment of the bulk modulus (see Figure 15) the following parameters were obtained Q=340kJ/mol, $\frac{\eta_0}{\alpha} = 0.021$, θ_c =0.6 and γ=1.24.

The actualize analytic model considering the grain growth on capillarity forces is

$$\dot{\theta} = \frac{-6(1-\theta)^3}{G\eta_0 Texp(\frac{Q}{RT})\psi} \quad (17)$$

The viscosity may also have a grain growth dependence in particle flattening or dissolution precipitation model [29] but our attempts to include this dependence results in too high a grain size sensitivity with an unrealistic behavior. Consequently, only the grain growth effect on the capillarity forces is modeled.

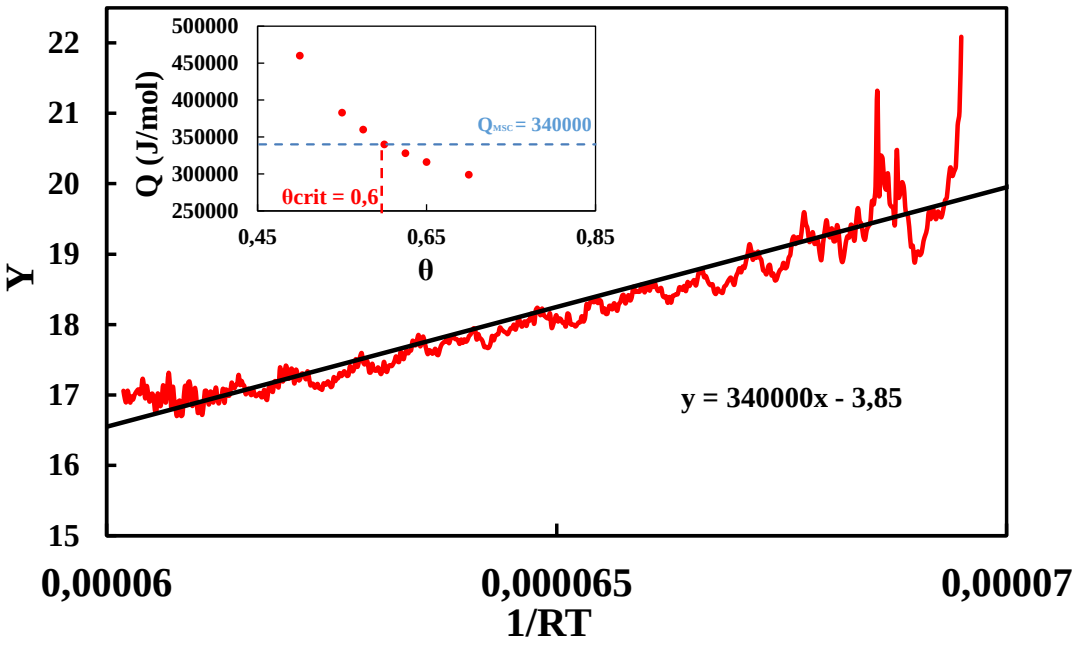

Figure 15 Linearization of Y for identification of $\frac{\eta_0}{\alpha}$knowing the adjusted apparent activation energy.

In an analogous case as the first model, using (17), it is now possible to plot the behavior of the material and compare it to experimental values (Figure 16). This second version fits experimental densification data in the open porosity zone until the pores close. Taking into account the pore swelling is visibly mandatory to model perfectly the behavior in the closed porosity zone.

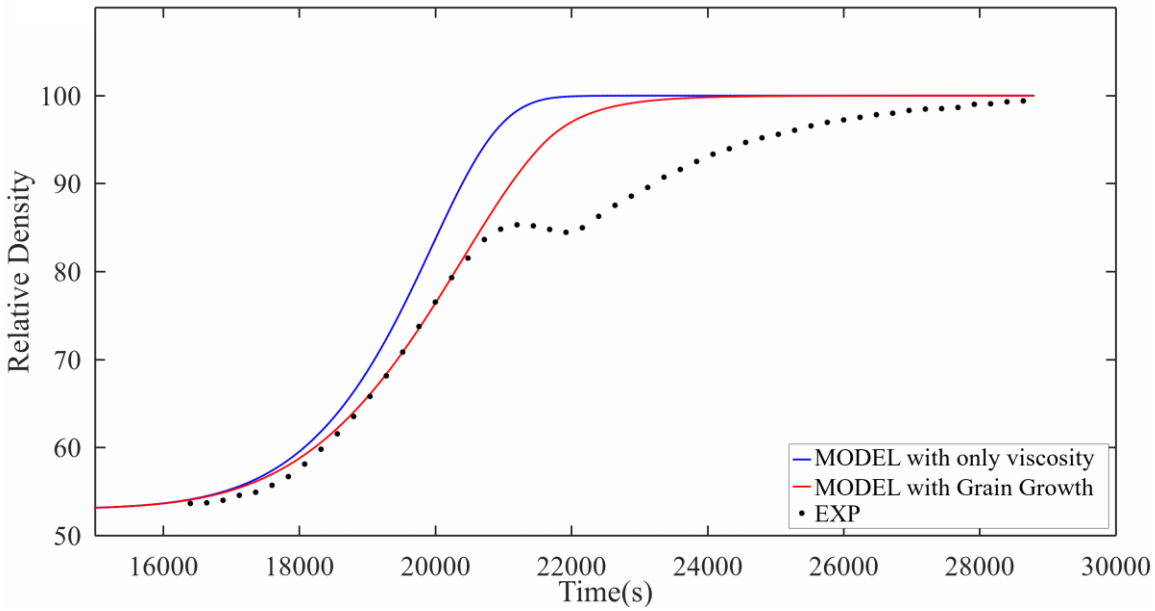

Figure 16 First and second sintering models and experimental values on Octave.

3.1.6. Case 3: Isotropic, Gas pressure sintering, with grain growth and pore swelling

This last case may take into account the gas trapped in the pores and the resulting pressure that could slow the densification. In this case the general model is taking into account more parameters. With Equation (1), the equivalent analytic model is the following

$$\dot{\theta} = \frac{(-Pl+Ps+\sigma_r)(1-\theta)}{\eta_0 T exp(\frac{Q}{RT})\psi(\theta)} \quad (18)$$

The latter analytical model takes into account the swelling pressure Ps which represents the swelling resulting pressure that opposes the sintering pressure Pl and the external applied gas pressure σ_r that help the porosity elimination at the final stage (~5 bar).

Using previous grain growth, and assuming previous viscosity and moduli identified in open porosity zone are the same in final stage sintering, and knowing the experimentally imposed gas pressure evolution (σ_r), the only unknown parameter is the experimental evolution of the swelling pressure Ps(t). With the final stage sintering shrinkage data, we can calculate the pore swelling by rearranging the model (18) by isolating the $\frac{Ps}{\alpha}$ ratio to be determined:

$$\frac{Ps}{\alpha} = \frac{\dot{\theta}\frac{\eta_0}{\alpha}Texp\left(\frac{Q}{RT}\right)\psi(\theta)}{(1-\theta)} + \frac{6(1-\theta)^2}{G} - \frac{\sigma_r}{\alpha} \quad (18)$$

In the last equation, the right part is already identified or can be calculated from the experimental data. The $\frac{Ps}{\alpha}$ evolution is reported in Figure 17a.

As depicted in the swelling phenomenon part, two mechanisms could be implied in this swelling. On one side, the pore inner pressure increases from the moment when the pores are pinched off. Pores may coalesce by partial solubility in the liquid phase and imply a swelling of the part until

it reaches a threshold. From this threshold, a part of the gas is being dissolved in liquid secondary phase, the swelling phenomenon slows and the densification starts again with the assistance of the furnace applied gas pressure (Figure 17 a.).

On the other side, this swelling can also be caused by the new generation of non-equiaxed grains (β) that have invaded the microstructure by being supplied by a generation of smaller equiaxed grains. Once this α/β allotropic transition is completed, the presence of a liquid phase at high temperature allows the densification to continue with a resorbing of the pores.

Interestingly, looking at Figure 17 b., we see that all the 3 heating rates seem to converge to a same pore swelling pressure of 6 MPa (assuming $\alpha \sim 1$). This pressure seems to be the inerrant material swelling pressure limits.

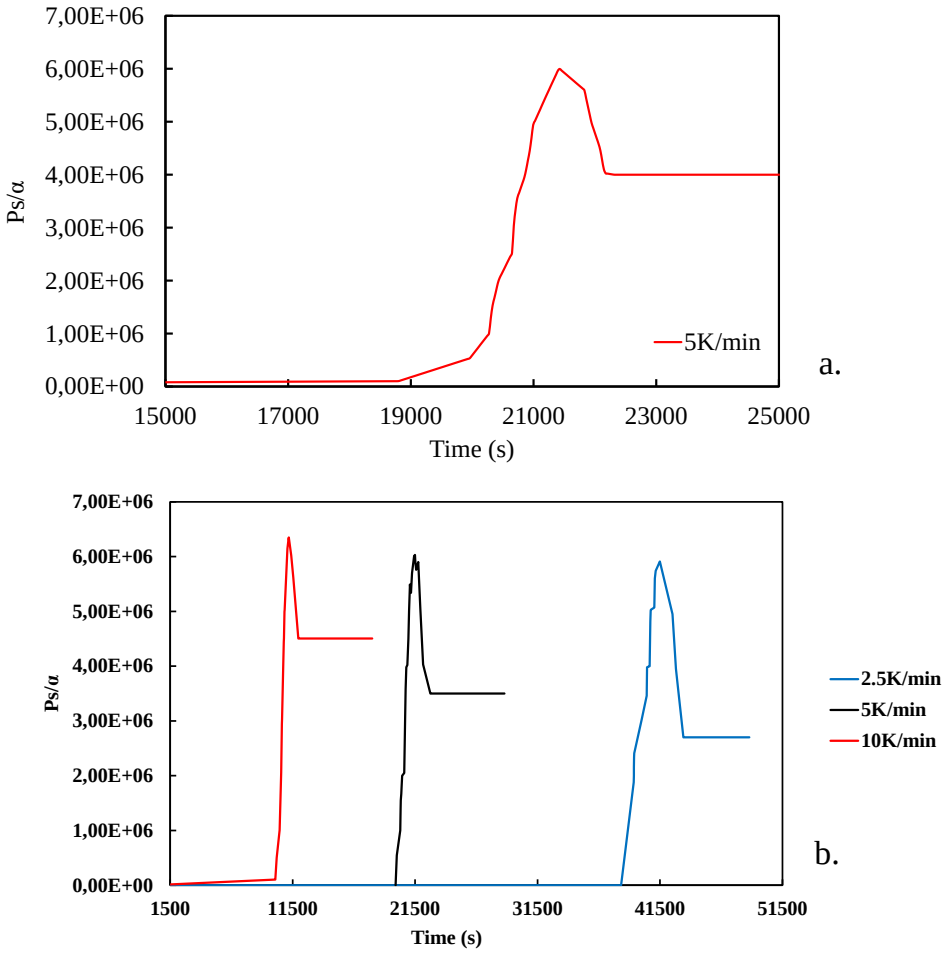

Figure 17 Pore swelling pressure as a function of time for the current study at 5K/min heating rate (a.) and comparison between 2,5K/min, 5K/min and 10K/min(b.).

This last model considers the parameters identified for the 2nd case and the swelling pressure that is opposing to the sintering forces[39]. The complete analytical model detailed below in green fits perfectly the experimental values (Figure 18).

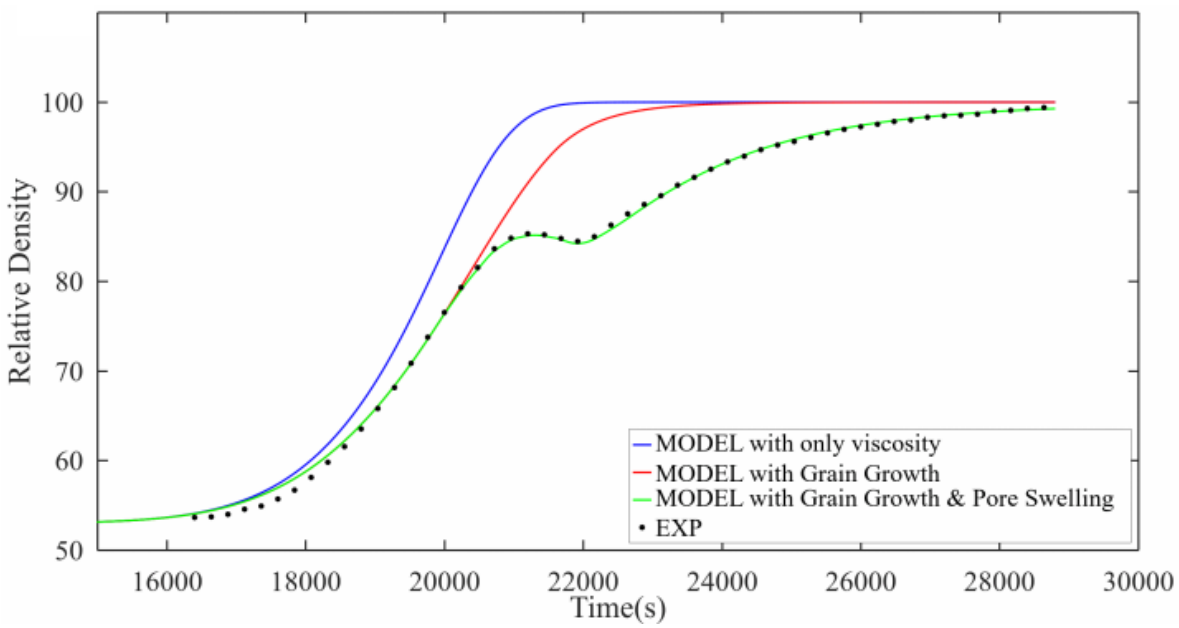

Figure 18 First, second and third sintering model and experimental values.

The model is now complete and able to predict the grain growth and swelling pressure behavior during sintering. It can be imported into a Finite Element modeling software to be applied to simulate 3D geometries.

4. Conclusion

Based on optical dilatometries and heating rate variations, it was possible to extract the complex sintering behavior of Si_3N_4 gas pressure liquid phase sintering. The formulation of the general equation of Skorohod-Olevsky's continuum theory of sintering has been the starting point of this study. The sintering exploration starts with a master sintering curve approach that helps characterizing the temperature behavior of the sintering. In final stage sintering, the densification of the powder is affected by the grain size, pore coalescence and/or non-equiaxial grain growth (linked to the α/β-Si_3N_4 allotropic transition) that both can generate a swelling phenomenon. The determination of the effective swelling pressure that opposes the sintering driving force is difficult and an invert method has been employed to identify experimentally the evolution of this function based on final stage sintering dilatometry. This study shows both grain growth and swelling phenomena modeling is mandatory to ensure a predictive sintering modeling of silicon nitride.

5. Acknowledgement

The author thanks Christelle Bilot for her help in the progression of this study. We would like to thank Thales Alenia Space for the PhD subvention of the author (CIFRE 2019/1366). A collaboration between four entities has been needed, FCTI (industry) has provided the debound specimens, the advanced gas sintering equipment of the Fraunhofer HTL has been used for the experimental sintering test, the modeling/simulation study is processed at the CRISMAT laboratory, and the assessment of the results for space applications is done by Thales Alenia Space. The help and support of Waldemar Walschewski is gratefully acknowledged.

6. Credit authorship contribution statement

Thomas Grippi: Conceptualization, Supervision, Experimentation, Modeling, Writing; **Stephanie Behar-Lafenetre:** Conceptualization, Supervision, Review & Editing; **Daniel Haas:** Experimentation, Review & Editing; **Uwe Schenderlein**: Experimentation, Review & Editing **Holger Friedrich:** Conceptualization, Experimentation, Supervision, Review & Editing; **Sylvain Marinel:** Supervision, Conceptualization, Review & Editing. **Charles Maniere:** Supervision, Conceptualization, Modeling, Writing, Review & Editing

7. References

[1] S. Behar-Lafenetre, N. Louh, P. Grasset, L. Cornillon, M. Such-Taboada, Silicon nitride for structural parts of space applications, in: B.A. Goodman, M. Kroedel (Eds.), Mater. Technol. Appl. to Opt. Struct. Components, Sub-Systems IV, SPIE, 2019: p. 3. https://doi.org/10.1117/12.2529078.

[2] L. Cornillon, C. Devilliers, S. Behar-Lafenetre, S. Ait-Zaid, K. Berroth, A.C. Bravo, Silicon nitride ceramic development in Thales Alenia Space : qualification achievement and further developments for future applications, in: B. Cugny, Z. Sodnik, N. Karafolas (Eds.), Int. Conf. Sp. Opt. — ICSO 2014, SPIE, 2017: p. 98. https://doi.org/10.1117/12.2304158.

[3] K.B. Christophe Devilliers, Thierry Lasic, David Boban, Laurence Cornillon, Dima Tanzilli, Sonia Aitzaid, Si3N4 ceramic application for large telescope development results, in: Int. Conf. Sp. Opt. 2012, 2017.
[4] T.G. Aguirre, C.L. Cramer, D.J. Mitchell, Review of additive manufacturing and densification techniques for the net- and near net-shaping of geometrically complex silicon nitride components, J. Eur. Ceram. Soc. 42 (2022) 735–743. https://doi.org/10.1016/j.jeurceramsoc.2021.11.001.
[5] X. Dong, J. Wu, H. Yu, Q. Zhou, W. Wang, X. Zhang, L. Zhang, L. Li, R. He, Additive manufacturing of silicon nitride ceramics: A review of advances and perspectives, Int. J. Appl. Ceram. Technol. 19 (2022) 2929–2949. https://doi.org/10.1111/ijac.14162.
[6] G. Petzow, M. Herrmann, Silicon Nitride Ceramics, in: Eng. Ceram. Curr. Status Futur. Prospect., 2002: pp. 47–167. https://doi.org/10.1007/3-540-45623-6_2.
[7] F.L. Riley, Silicon Nitride and Related Materials, J. Am. Ceram. Soc. 83 (2004) 245–265. https://doi.org/10.1111/j.1151-2916.2000.tb01182.x.
[8] L.J. Bowen, R.J. Weston, T.G. Carruthers, R.J. Brook, Hot-pressing and the α-β phase transformation in silicon nitride, J. Mater. Sci. 13 (1978) 341–350. https://doi.org/10.1007/BF00647779.
[9] L.J. BOWEN, T.G. CARRUTHERS, R.J. BROOK, Hot-Pressing of Si3N4 with Y2O3 and Li2O as Additives, J. Am. Ceram. Soc. 61 (1978) 335–359. https://doi.org/10.1111/j.1151-2916.1978.tb09323.x.
[10] O.A. Lukianova, V.Y. Novikov, A.A. Parkhomenko, V. V. Sirota, V. V. Krasilnikov, Microstructure of Spark Plasma-Sintered Silicon Nitride Ceramics, Nanoscale Res. Lett. 12 (2017) 0–5. https://doi.org/10.1186/s11671-017-2067-z.
[11] M. Mitomo, N. Yang, Y. Kishi, Y. Bando, Influence of powder characteristics on gas pressure sintering of Si3N4, J. Mater. Sci. 23 (1988) 3413–3419. https://doi.org/10.1007/BF00551328.
[12] M. Mitomo, Pressure sintering of Si3N4, J. Mater. Sci. 11 (1976) 1103–1107. https://doi.org/10.1007/BF02396645.
[13] Z. Huang, L. Wu, Phase equilibria diagrams of high-temperature non-oxide ceramics, 2018. https://doi.org/10.1007/978-981-13-0463-7.
[14] R.C. Lange, F.F., Singhal, S.C., and Kuznicki, Phase relations and stability studies in the Si3 N4–SiO2–Y2O3 pseudoternary, J. Am. Ceram. Soc., 60, 249. (1977).
[15] F.F. Lange, Phase relations in the system Si3 N4–SiO2 –MgO and their interrelation with strength and oxidation, J. Am. Ceram. Soc. (1978) 53.
[16] V. V Krasil, V. V Sirota, A.S. Ivanov, L.N. Kozlova, O.A. Luk, INVESTIGATION OF THE STRUCTURE OF Si 3 N 4 -BASED CERAMIC WITH Al 2 O 3 AND Y 2 O 3 ADDITIVES, 71 (2014) 15–17.
[17] Y. Tajima, Development of High Performance Silicon Nitride Ceramics and their Applications, MRS Proc. 287 (1992) 189. https://doi.org/10.1557/PROC-287-189.
[18] F. Zhou, J. Pan, K. Chen, Liquid-phase bonding of silicon nitride ceramics using Y2O 3-Al2O3-SiO2-TiO2 mixtures, Mater. Lett. 58 (2004) 1383–1386. https://doi.org/10.1016/j.matlet.2003.09.032.
[19] N. Liu, J. Zhang, Y. Duan, X. Li, S. Dong, Effect of rare earth oxides addition on the mechanical properties and coloration of silicon nitride ceramics, J. Eur. Ceram. Soc. 40 (2020) 1132–1138. https://doi.org/10.1016/j.jeurceramsoc.2019.11.058.
[20] J. Liu, R.M. German, Densification and shape distortion in liquid-phase sintering, Metall.

Mater. Trans. A Phys. Metall. Mater. Sci. 30 (1999) 3211–3217. https://doi.org/10.1007/s11661-999-0231-5.
[21] S.J. Park, P. Suri, E. Olevsky, R.M. German, Master sintering curve formulated from constitutive models, J. Am. Ceram. Soc. 92 (2009) 1410–1413. https://doi.org/10.1111/j.1551-2916.2009.02983.x.
[22] R. Bollina, S.J. Park, R.M. German, Master sintering curve concepts applied to full-density supersolidus liquid phase sintering of 316L stainless steel powder, Powder Metall. 53 (2010) 20–26. https://doi.org/10.1179/174329009X409688.
[23] J. Wang, R. Raj, Estimate of the Activation Energies for Boundary Diffusion from Rate-Controlled Sintering of Pure Alumina, and Alumina Doped with Zirconia or Titania, J. Am. Ceram. Soc. 73 (1990) 1172–1175. https://doi.org/10.1111/j.1151-2916.1990.tb05175.x.
[24] F. Raether, P. Schulze Horn, Investigation of sintering mechanisms of alumina using kinetic field and master sintering diagrams, J. Eur. Ceram. Soc. 29 (2009) 2225–2234. https://doi.org/10.1016/j.jeurceramsoc.2009.01.025.
[25] F. Raether, R. Springer, S. Beyer, Optical dilatometry for the control of microstructure development during sintering, Mater. Res. Innov. 4 (2001) 245–250. https://doi.org/10.1007/s100190000101.
[26] H. Su, D.L. Johnson, Master Sintering Curve: A Practical Approach to Sintering, J. Am. Ceram. Soc. 79 (1996) 3211–3217. https://doi.org/10.1111/j.1151-2916.1996.tb08097.x.
[27] S.M. Charles Maniere, Thomas Grippi, Estimate microstructure development from sintering shrinkage: A kinetic field approach, Mater. Today Commun. 31 (2022).
[28] G. Kerbart, C. Manière, C. Harnois, S. Marinel, Master sintering curve with dissimilar grain growth trajectories: A case study on MgAl2O4, J. Eur. Ceram. Soc. 41 (2021) 1048–1051. https://doi.org/10.1016/j.jeurceramsoc.2020.09.003.
[29] Mohamed N. Rahaman, Sintering of Ceramics, in: Sinter. Ceram., CRC Press, 2007: pp. 1–43. https://doi.org/10.1201/b15869-2.
[30] C. Manière, C. Harnois, S. Marinel, 3D printing of porcelain and finite element simulation of sintering affected by final stage pore gas pressure, Mater. Today Commun. 26 (2021). https://doi.org/10.1016/j.mtcomm.2021.102063.
[31] F.C. Peillon, F. Thevenot, Grain coarsening in gas pressure sintered silicon nitride, Ceram. Int. 28 (2002) 637–643. https://doi.org/10.1016/S0272-8842(02)00020-2.
[32] H. Emoto, M. Mitomo, Control and characterization of abnormally grown grains in silicon nitride ceramics, J. Eur. Ceram. Soc. 17 (1997) 797–804. https://doi.org/10.1016/s0955-2219(96)00139-2.
[33] M. Demartin, C. Hérard, C. Carry, J. Lemaître, Dedensification and anomalous grain growth during sintering of undoped barium titanate, J. Am. Ceram. Soc. 80 (1997) 1079–1084. https://doi.org/10.1111/j.1151-2916.1997.tb02949.x.
[34] C. Chambon, S. Vaudez, J.M. Heintz, De-densification mechanisms of yttria-doped cerium oxide during sintering in a reducing atmosphere, J. Am. Ceram. Soc. 101 (2018) 4956–4967. https://doi.org/10.1111/jace.15741.
[35] V.V. Skorohod, Rheological basis of the theory of sintering, Nauk. Dumka, Kiev. (1972).
[36] T. Grippi, S. Béhar-Lafenetre, H. Friedrich, D. Haas, U. Schenderlein, S. Marinel, C. Manière, Grain growth modeling for gas pressure sintering of silicon nitride based ceramics, Mater. Today Commun. 34 (2023). https://doi.org/10.1016/j.mtcomm.2022.105189.
[37] E.A. Olevsky, Theory of sintering: From discrete to continuum, Mater. Sci. Eng. R Reports. 23 (1998) 41–100. https://doi.org/10.1016/S0927-796X(98)00009-6.

[38] C. Manière, G. Lee, J. McKittrick, S. Chan, E.A. Olevsky, Modeling zirconia sintering trajectory for obtaining translucent submicronic ceramics for dental implant applications, Acta Mater. 188 (2020) 101–107. https://doi.org/10.1016/j.actamat.2020.01.061.
[39] C. Manière, E. Saccardo, G. Lee, J. McKittrick, A. Molinari, E.A. Olevsky, Swelling negation during sintering of sterling silver: An experimental and theoretical approach, Results Phys. 11 (2018) 79–84. https://doi.org/10.1016/j.rinp.2018.08.035.